communications earth & environment

Article

https://doi.org/10.1038/s43247-024-01628-9

Eocene maar sediments record warming of up to 3.5 °C during a hyperthermal event 47.2 million years ago

Clemens Schmitt[1,2] ✉, Iuliana Vasiliev[1], Niels Meijer[1], Julia Brugger[1], Stefanie Kaboth-Bahr[3], André Bahr[4] & Andreas Mulch[1,2]

Eocene hyperthermal events reflect profound perturbations of the global carbon cycle. Most of our knowledge about their onset, timing, and rates originates from marine records. Hence, the pacing and magnitude of hyperthermal continental warming remains largely unaccounted for due to a lack of high-resolution climate records. Here we use terrestrial biomarkers and carbon isotopes retrieved from varved lake deposits of the UNESCO World Heritage site 'Messel Fossil Pit' (Germany) to quantify sub-millennial to millennial-scale temperature and carbon isotope changes across hyperthermal event C21n-H1 (47.2 million years ago). Our results show maximum warming of ca. 3.5 °C during C21n-H1. We propose that two components are responsible for the warming pattern across the hyperthermal: (1) the massive release of greenhouse gases into the atmosphere-ocean system and (2) half-precession orbital forcing indicated by ~12.000-year temperature cycles. The carbon isotope record of bulk organic matter indicates a sharp, 7‰ decrease at the peak of the hyperthermal, corresponding to increased organic carbon content and a shift in the lake algal community. Collectively, our proxy data reveal the structure of continental temperature response during the hyperthermal event that is characterized by overall warming with a superimposed pattern of sub-orbital scale temperature fluctuations.

A sequence of short-lived (10^4–10^5 ka) perturbations of the global carbon cycle associated with massive injections of ^{13}C-depleted greenhouse gases into the atmosphere-ocean system (hyperthermal events) culminated in episodic global warming during the early and middle Eocene[1–3] (~56–46 Ma). These carbon cycle perturbations resulted in negative carbon isotope excursions (CIEs) recorded in terrestrial and marine geological archives[4–6] revealing fundamental changes in ocean circulation and chemistry including acidification and carbonate dissolution[3]. While the timing of such hyperthermals can be reconstructed in marine (carbonate) records[7–9] the amplitude and pacing of temperature change during such hyperthermals remains poorly constrained, due to a lack of continuous high-resolution hyperthermal records. To date, only the Paleocene–Eocene Thermal Maximum (PETM; ~56 Ma) has been well-documented[10,11], with global surface warming estimated to have been between 5.0 °C and 5.6 °C[12,13]. The PETM however, was extreme in its magnitude of warming, duration, and environmental impact[14] compared to the numerous smaller orbitally-paced early to middle Eocene (~54–46 Ma) hyperthermals and associated CIEs[5]. These post-PETM CIEs, are nonetheless a recurring characteristic feature of the Eocene greenhouse climate over several million years[5] but their temperature response is still underexplored, especially in continental environments. This shortcoming generally limits our ability to project knowledge of abrupt temperature perturbations in the past to analogous scenarios predicted for future global warming[15]. Particularly high-resolution (varved) terrestrial proxy temperature records provide valuable insights into short-term (sub-millennial to millennial) temperature change and climate feedbacks during such hyperthermals and moreover, offer unique opportunities to resolve the rate of warming during these events.

Here, we use branched glycerol dialkyl glycerol tetraethers (brGDGTs) and stable carbon isotopic compositions of total organic matter (OM) ($\delta^{13}C_{TOC}$) from the varved maar lake succession of the UNESCO World Heritage Site 'Messel Fossil Pit' (Germany; Fig. 1) to quantify sub-millennial to millennial-scale mid-latitude continental mean annual air temperature (MAT) change across the C21n-H1 hyperthermal (47.2 Ma). We show that

[1]Senckenberg Biodiversity and Climate Research Centre, Frankfurt, Germany. [2]Goethe University Frankfurt, Institute of Geosciences, Frankfurt, Germany. [3]Institute of Geological Sciences, Freie Universität Berlin, Berlin, Germany. [4]Institute of Earth Sciences, Heidelberg University, Heidelberg, Germany. ✉e-mail: clemens.schmitt@senckenberg.de

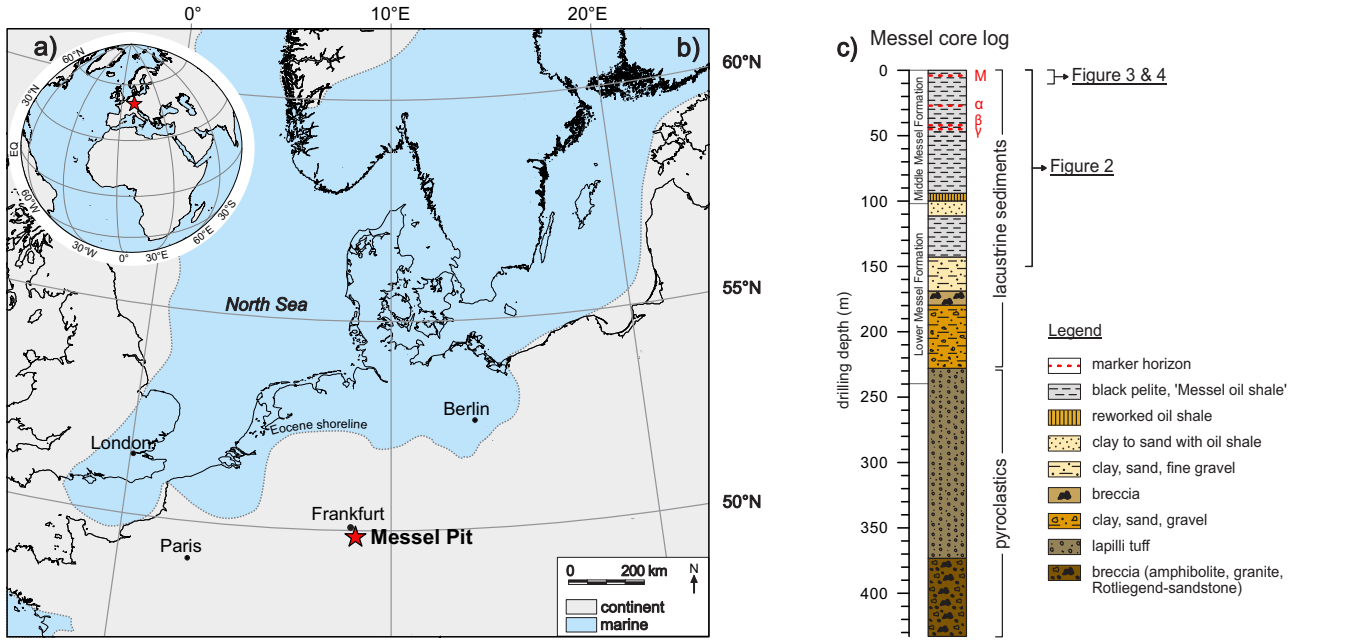

Fig. 1 | Location of Messel study site and Messel drill core. a Location of the Messel UNESCO World Heritage site. **b** Present-day geography of Central Europe overlain by reconstructed early Eocene land–sea distribution[66,67]. Red star locates present-day location (WGS 84: 49.915° N, 8.7513° E). Eocene Messel maar position was ~46–47° N[46]. **c** Generalized lithological units of the FB2001 Messel core[25] with marker horizons (M, α, β, and γ) indicated by dashed red lines[25].

a pronounced rise in continental temperature also accompanies the less pronounced Eocene CIEs recorded in the deep ocean. In addition, our data suggest that warming was modulated by and perhaps amplified by orbital forcing. Further, Messel proxy temperatures prior to the event match best Eocene model simulations of the Deep-Time Model Intercomparison Project (DeepMIP) under four-fold pre-industrial pCO_2 concentrations. The temperature rise during the hyperthermal event recorded by the brGDGT-proxy is consistent with a pCO_2 increase of less than a doubling from background levels in the DeepMIP models. Moreover, carbon cycling within the lake experienced strong alterations during the peak of the hyperthermal. These changes were associated with a turnover in predominant algal communities probably due to changing environmental and limnological conditions.

Results

Structure of the hyperthermal, carbon isotope pattern, and total organic carbon (TOC) content

Based on our high-resolution $\delta^{13}C_{TOC}$ (Figs. 2 and 3) and biomarker-derived temperature record, we structure hyperthermal C21n-H1 into (1) pre-Event (ending at 47.26 Ma), (2) peak-Event indicated by decreasing $\delta^{13}C_{TOC}$ and warmest temperatures (47.26–47.24 Ma), (3) Recovery indicated by increasing $\delta^{13}C_{TOC}$ and cooling (47.24–47.23 Ma), and (4) post-Event (starting at 47.23 Ma) intervals (Figs. 3 and 4). During the CIE, we further detect an abrupt and rapid increase in TOC corresponding to a decrease in $\delta^{13}C_{TOC}$ at 47.24 Ma, collectively interpreted as a local disturbance in lake carbon reservoirs during peak hyperthermal conditions (see "Discussion").

Throughout the hyperthermal, the $\delta^{13}C_{TOC}$ record varies by 10‰ ranging from −25.1‰ to −35.1‰ (Fig. 3). Pre-Event values are constant at −29‰ ($n = 4$), closely clustering to the mean (−28.3‰; $n = 90$) of the long-term (47.9 Ma to 47.3 Ma) $\delta^{13}C_{TOC}$ Messel record prior to C21n-H1 (Fig. 2). After a $\delta^{13}C_{TOC}$ increase (from ca. −29‰ to −25‰) at the transition from the pre-Event to the peak-Event interval, $\delta^{13}C_{TOC}$ values gradually decrease by 3.2‰, from −26.7‰ to −29.5‰ through the peak-Event interval. This overall decreasing trend is punctuated by fluctuations of 1‰ to 2‰ (Fig. 3). A rapid decrease in $\delta^{13}C_{TOC}$ of ~7‰ from −28.3‰ to −35.2‰ coincides with TOC increase to ca. 50% (Fig. 3). Within the Recovery interval, $\delta^{13}C_{TOC}$ values remain low compared to the peak-Event interval, but increase by ~4‰ from −34‰ to −30‰ throughout the end of the latter. TOC values vary by ~15% (~30–45%) during the peak-Event interval, yet exhibit high (~40–55%) values in the Recovery interval before they decrease to ca. 40% in the post-Event interval (Fig. 3).

Temperature evolution

Within the hyperthermal, brGDGT MATs vary between 22.5 and 28.0 °C (calibration error: ±2.9 °C; Fig. 3 and Table 1). Pre-Event temperatures are stable (23.8–25.2 °C; $n = 2$) but increase by ~2.5 °C from 25.5 °C to 28.0 °C at the beginning of the peak-Event interval at 47.25 Ma. Following this first temperature maximum, a gradual ~3 °C cooling to 25.0 °C predates a second warming phase of 2.5 °C (from 25.0 °C to 27.5 °C) at 47.24 Ma (Figs. 3 and 4). After a rapid 3.0 °C temperature decrease (27.5–24.5 °C) accompanying the local carbon disturbance, an overall cooling trend of 3.6 °C (from 26.2 °C to 22.6 °C), albeit with temperature fluctuations is observed across the Recovery interval. Post-Event temperatures range between 23.7 °C and 25.1 °C ($n = 4$) (Fig. 3 and Table 1).

Discussion

Age control and identification of hyperthermal event C21n-H1

Based on the gamma-ray record of the Messel drill core (FB2001), which traces variable detrital input to the lake system due to orbitally-driven changes in precipitation[16] a recently developed astronomically tuned age model (Fig. 2) places the Middle Messel Formation (MMF; Fig. 1c) between 47.65 Ma and 47.22 Ma. Thus, the MMF covers a ~430 ka time interval, comprising hyperthermal event C21n-H1 in the upper 12 m of the cored MMF. C21n-H1, initially documented in Pacific ODP Site 1209[5], was later also identified in the Atlantic ODP Site 1263[6] (Fig. 2a). At Messel, the identification of C21n-H1 between ~1 m and 8 m core depth of the MMF (Supplementary Fig. 1) is based on a negative CIE in the bulk OM starting at 47.26 Ma. According to the astronomical tuning of the Messel core[16], which is independent of the global benthic $\delta^{13}C$ stack (CENOGRID), the studied CIE correlates with the hyperthermal detected in the benthic $\delta^{13}C$ at 47.2 Ma (Fig. 2).

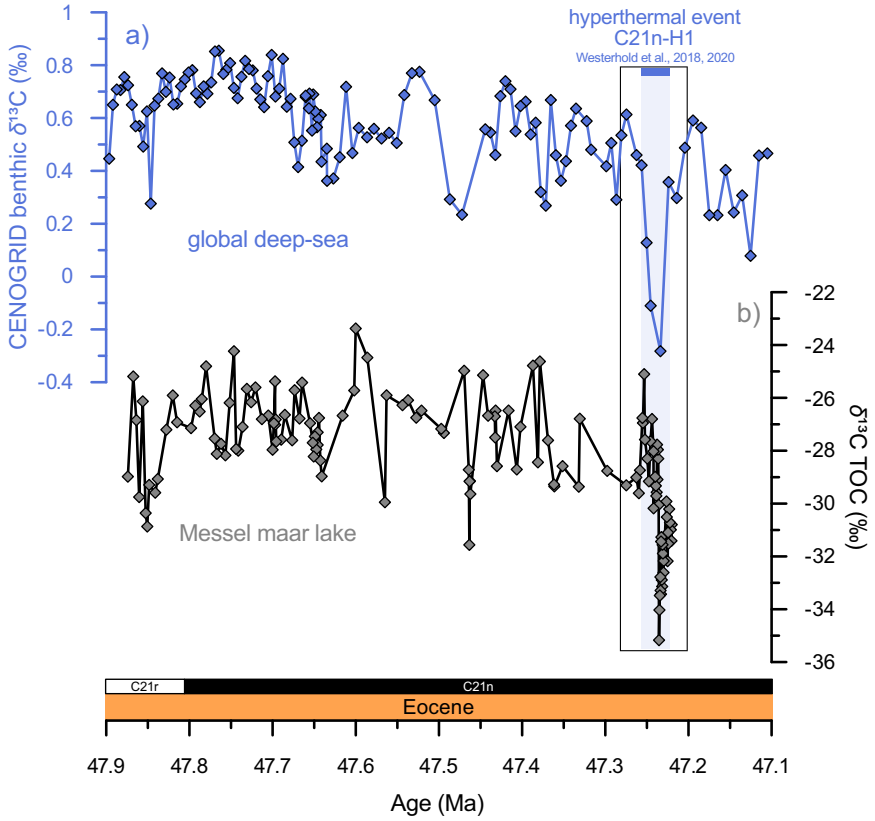

Fig. 2 | Comparison of global marine and Messel carbon records. a Global benthic $\delta^{13}C$ stack (CENOGRID[6]) and **b** composite Messel $\delta^{13}C_{TOC}$ record from this study and[16,32] (Supplementary Data) for the uppermost 150 m of core FB2001 (see Fig. 1c). Black rectangle indicates hyperthermal sequence shown in Figs. 3 and 4.

Fidelity of the brGDGT-based temperature record

Molecular organic compounds in Messel maar sediments were among the earliest to examine deep-time paleoenvironmental conditions, particularly due to their variety and excellent preservation[17,18]. Time-continuous temperature reconstructions throughout the Messel core based on brGDGT paleothermometry have, however, been lacking. While ambient temperature exerts a strong control on the distribution of brGDGTs in lakes[19,20] (expressed by the MBT'$_{5Me}$ index, Eq. 1), other environmental parameters such as e.g., water chemistry, oxygen availability, or vegetation could bias the MBT'$_{5Me}$–temperature relationship[21–23]. Through the hyperthermal section of the core, CBT'-derived (Eq. 2) water pH estimates (Eq. 3) vary between 7.6 and 6.9 (Fig. 3) and do not correlate with temperature changes. Further, no significant changes in vegetation composition[24] or lithofacies[25] (Supplementary Fig. 2) have been reported during the hyperthermal event. We, therefore, argue that the aforementioned parameters had negligible impact on brGDGT paleothermometry that if at all, would result in a temperature bias that is likely smaller than the calibration error. However, substantial shifts in the microbial community due to limnological changes such as increased overturning and/or stratification[26,27] or enhanced influx of soil-derived brGDGTs into the lake with a distinct brGDGT distribution[20,28,29] could bias the recovered temperature data. Seasonal lake mixing in a tropical East African crater lake (Lake Chala) has been shown to affect the brGDGT-producing bacterial community composition due to shallowing of the oxic-anoxic boundary[26]. Such short-term mixing events, if present at Messel, are unlikely to significantly alter the MBT'$_{5Me}$–temperature relation, since each sample analyzed integrates ≥ 25 years, based on an estimated sedimentation rate of 0.2 mm per year at Messel[16]. However, we do acknowledge that multi-decadal cyclicity (52 years and 82 years) has been recorded in the varved sedimentary record of the Messel core[30]. Nevertheless, variable dissolved oxygen concentrations within the water column associated with lake overturning are suggested to have minor effects on the MBT'$_{5Me}$ index[31]. Lastly, we assume that the majority of the brGDGTs were produced within the lake, although allochthonous OM has been deposited at Messel[32]. This assumption is supported by (1) low scatter in IIIa/IIa ratio (Supplementary Fig. 1), which indicates no major shifts in brGDGT sourcing, (2) high lake productivity with bottom anoxia that may support growth of heterotrophic brGDGT-producing bacteria[33,34], and (3) a small to almost absent catchment area that was composed only of local, lapilli tuff crater walls, therefore limiting erosional input due to absence of riverine input[35].

Temperature variability during hyperthermal event C21n-H1

Major changes in brGDGT-based temperatures during C21n-H1 correlate with coeval shifts in ocean chemistry and the global carbon cycle, indicating strong ocean-land connectivity through the hyperthermal. Specifically, brGDGT temperatures are on average ~2°C (n = 14) higher within the peak-Event interval relative to average pre- and post-Event temperatures (Fig. 4h and Table 1). Since average pre- and post-Event temperatures are equal (24.5 °C; n = 2 and 24.4 °C; n = 4, respectively) we claim that temperatures returned to initial (pre-Event) levels after the hyperthermal. Although only a limited number of brGDGT-based pre-Event temperatures are available (n = 2) these estimates are only slightly higher than MATs at Messel obtained by leaf margin analysis (21.7 ± 1.8–23.1 ± 1.9 °C) or the paleobotanical coexistence approach (16.8–23.9 °C) from fossil plant material prior to the hyperthermal[36]. Hence, we argue that the pre-Event temperatures presented here reflect a plausible estimate of the background climate state at Messel just before the onset of the hyperthermal. Relative to the average pre- and post-Event temperatures (24.4 °C; n = 6), maximum warming across the C21n-H1 hyperthermal is ca. 3.5 °C (Fig. 4h). Notably, the pacing of continental hyperthermal warming from ~47.25 Ma to 47.24 Ma over a duration of ~8900 years (Fig. 4c) implies an average rate of warming of ~0.4°C per thousand years, which is approximately two orders of magnitude lower than the current rate of global warming (global continental temperatures in 2011–2022 ~ 1.6 °C above 1850–1900)[37]. The duration of stepwise cooling during the Recovery phase (~47.23 Ma to 47.22 Ma over ~9800 years; Fig. 4c) is similar to the warming. This suggests a relatively rapid (~10 ka) removal of greenhouse gases after the hyperthermal event,

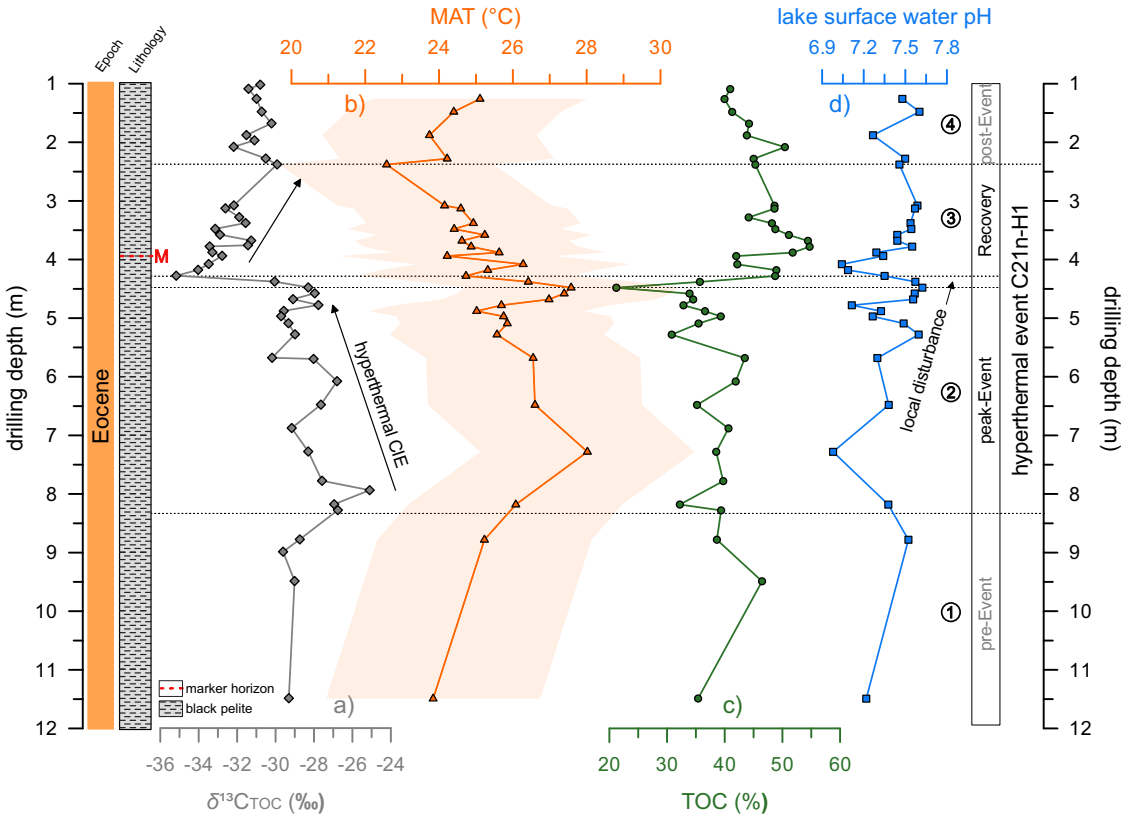

Fig. 3 | High-resolution proxy records through hyperthermal event C21n-H1. a $\delta^{13}C$ values of bulk OM ($\delta^{13}C_{TOC}$), **b** brGDGT-based MATs. Orange shading indicates RMSE uncertainty (±2.9 °C). **c** TOC content, and **d** surface water pH estimates within the top 12 m of core FB2001 including the hyperthermal interval (~8.5–2.5 m).

which might be related to accelerated carbon sequestration as it has been inferred for several early Eocene hyperthermals (e.g., event I1, H2)[38]. Furthermore, our high-resolution temperature record reveals short-term (sub-millennial to millennial) MAT variability of up to 3 °C and ~3 °C gradual cooling between two warming periods within the peak-Event interval (at 47.25 Ma and 47.24 Ma). This gradual cooling does not correlate with significant changes in lithofacies[25], vegetation composition, input of OM[24], or lake pH (Fig. 3) and we do not find evidence for non-thermal effects on the MAT signal[39].

Increases in global temperatures during hyperthermals are generally attributed to the large-volume release of ^{13}C-depleted greenhouse gases into the ocean-atmosphere system[2,3]. However, superimposed short-term temperature fluctuations might also be directly driven by changes in orbital parameters[40]. Model simulations indicate that orbital forcing could have amplified seasonal surface air temperature increase during past greenhouse climates[40,41]. We note that warming maxima in the Messel record are separated by ~12–20 ka during the peak-Event and post-Event at ~47.25 Ma, 47.24 Ma, and 47.22 Ma, respectively. The pacing of these warming events corresponds to half-precession and precession cycles, respectively, both previously reported in the Messel record[16,42]. Half-precession signals (~9–12 ka) are typically most pronounced at low-latitudes[43,44], but have also been recognized in mid-latitude interglacials (Lake Ohrid, Balkan) due to an intensified lower latitude monsoon system[45]. We, therefore, hypothesize, that intensification of northward atmospheric/oceanic transport between the tropics and Eocene mid-latitudes with the Messel Maar lake at ca. 46–47° N[46], could have facilitated warm tropical airmasses propagating northward on half-precession timescales thereby amplifying the warming maxima during the hyperthermal.

We note that a similar sub-orbital cyclicity has been observed in the pollen record (*Pityosporites labdacus*)[42]. The structure of the *P. labdacus* record throughout C21n-H1 is remarkably consistent with the brGDGT MAT estimates as both warming peaks are mirrored by high *P. labdacus* abundance (Supplementary Fig. 1c), hence supporting our hypothesis of orbitally amplified maximal temperatures during C21-nH1. We are unable to separate warming associated with the hyperthermal-induced greenhouse forcing from half-precession forcing based on our brGDGT dataset alone. Yet, model simulations across the PETM indicate up to ~6 °C mean annual surface warming in the northern hemisphere mid-latitudes under maximum orbital configurations compared to minimum orbital insolation[40].

An Eocene maar record of global and local carbon cycle perturbation

Comparison of the high-resolution Messel $\delta^{13}C_{TOC}$ record with the CENOGRID marine benthic $\delta^{13}C$ stack shows a coeval $\delta^{13}C_{TOC}$ decrease (from −26.7‰ to −29.5‰) during the peak-Event (~47.26–47.24 Ma), a $\delta^{13}C_{TOC}$ minimum (−35.2‰) at ~47.24 Ma and gradual ^{13}C-enrichment across the Recovery interval (~47.24–47.23 Ma) (Fig. 4). Notably, $\delta^{13}C_{TOC}$ values as low as −35.2‰ are not reported at any time prior the hyperthermal event throughout the Messel core covering ~650 ka (Fig. 2), thus indicating fundamental changes within lake carbon reservoir during C21n-H1. The consistent pacing and direction of change between both, global marine and mid-latitude continental (Messel maar lake) $\delta^{13}C$ records collectively suggest a global carbon cycle imprint recorded in the maar sediments. However, since the OM in the Messel maar deposits is composed of autochthonous and allochthonous sources[32] additional site-specific factors likely played a role[4,47,48]. Short-term fluctuations of the Messel $\delta^{13}C_{TOC}$ record (e.g., peak-Event interval) that deviate from long-term global trends during the hyperthermal most likely reflect changing lake conditions associated with e.g., variable past productivity rates or changes in partitioning of the source of OM[48,49]. For example, compound-specific $\delta^{13}C$ measurements of algae and photosynthetic bacteria from Messel maar pelites revealed comparatively high $\delta^{13}C$ values (−22.5‰ and −24.5‰, respectively)[17,50]. Hence, a higher contribution of algal biomass to the total OM has been inferred as responsible for short-term carbon excursions towards more ^{13}C-enriched

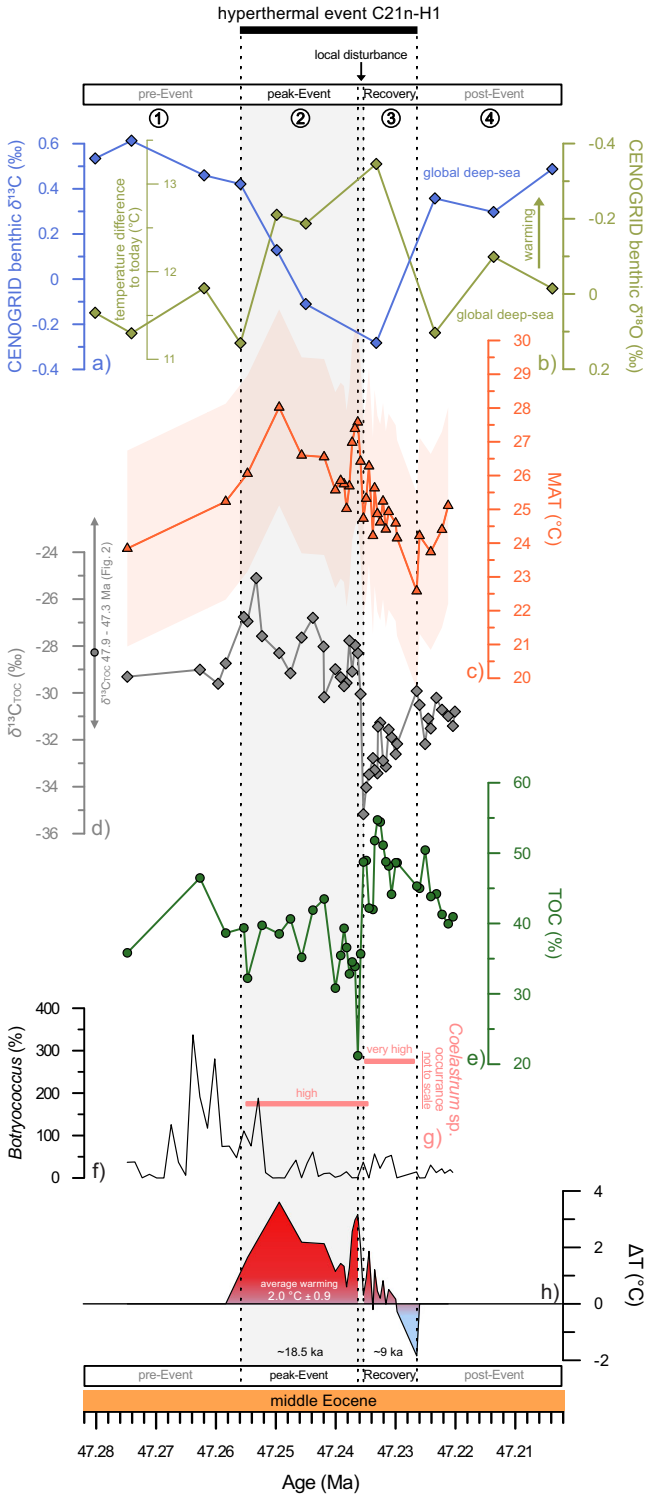

Fig. 4 | Composite global marine and Messel proxy records through hyperthermal event C21n-H1. a Benthic $\delta^{13}C$ and **b** $\delta^{18}O$ records (CENOGRID) from ODP site 1263[6]. **c** Messel FB2001 brGDGT-based MAT reconstruction. Orange shading indicates RMSE uncertainty (±2.9 °C). **d** Composite Messel FB2001 $\delta^{13}C_{TOC}$ record[16,32] and this study (Supplementary Data). The arrow represents the $\delta^{13}C_{TOC}$ range between 47.9 Ma and 47.3 Ma, and the gray dot represents the mean $\delta^{13}C_{TOC}$. **e** Messel FB2001 TOC content (%). **f** Abundance of *Botryococcus braunii*. *B. braunii* percentage calculations follows[42]. **g** Abundance of *Coelastrum sp*[54]. **h** brGDGT-based temperature difference ± standard deviation between average pre-/post-Event and hyperthermal peak-Event/Recovery.

Table 1 | Temperatures from Messel and global $\delta^{13}C_{benthic}$ throughout hyperthermal C21n-H1

Parameter	Pre-Event	Peak-Event	Recovery	Post-Event
MAT (°C)	23.8–25.2 (±2.9)	25.5–28.0 (±2.9)	22.5–26.2 (±2.9)	23.7–25.1 (±2.9)
avg. MAT (°C)	24.5 (n = 2)	26.4 (n = 12)	24.7 (n = 13)	24.4 (n = 4)
avg. ΔT (°C)[a]	Reference T	2.0	0.3	Reference T
$\delta^{13}C_{benthic}$ (‰)[b]	0.61–0.42	0.12 to −0.11	−0.28	0.29–0.48

[a]ΔT is normalized to average pre- and post-Event temperatures (24.4 °C).
[b]Values from CENOGRID[6].

values within the MMF[32]. We, therefore, propose that the rapid $\delta^{13}C_{TOC}$ decrease of ~7‰ at ~47.24 Ma and the subsequent recovery were at least in part controlled by perturbations of lake internal carbon reservoirs such as changes in primary productivity and planktonic community. The latter has been shown to account for $\delta^{13}C_{TOC}$ shifts of up to 9‰ in comparable Holocene maars (Lake Holzmaar, Germany)[51]. Primary productivity seems to have been enhanced at the beginning of the peak-Event interval, as suggested by the increasing presence of *Botryococcus braunii* algae (with $\delta^{13}C_{B.braunii}$ of −10‰ to −23‰[32,52]), potentially biasing the $\delta^{13}C_{TOC}$ towards less negative values and causing the ~2‰ increase in $\delta^{13}C_{TOC}$ at 47.26 Ma (Fig. 3). *B. braunii* becomes less abundant during the peak-Event interval (Fig. 4), whereas *Coelastrum sp*. algae (whose occurrence has been documented to coincide with more negative $\delta^{13}C_{TOC}$ values[53]) becomes highly abundant, at the local disturbance and during the Recovery interval (Fig. 4)[54]. We, therefore, suggest that a shift in algal communities characterized by different $\delta^{13}C$ values was associated with the large magnitude $\delta^{13}C_{TOC}$ decrease at 47.24 Ma. This suggestion is supported by a higher loading of phytoplankton to the sediments derived from enhanced hydrogen index values across the Recovery interval[32]. This interval also correlates with a ~15% increase in TOC, possibly associated with a combination of improved OM preservation, higher OM production, and/or less clastic input from the crater rim (Figs. 3 and 4). Alternatively, hydroclimatic changes, suggested to be regionally pronounced during Eocene warming intervals[55] could have triggered lake level fluctuations and, in turn, promoted the release of ^{13}C-depleted gases (e.g., CH_4) from buried OM[56,57]. However, stable isoGDGT-0/Crenarchaeol ratios suggest that methanogenic activity likely did not change notably during the rapid $\delta^{13}C_{TOC}$ decrease, even though these values should be taken with caution considering low Crenarchaeol amplitudes within the MMF (Supplementary Fig. 1).

Finally, we compare brGDGT-derived continental temperatures with Eocene surface air temperatures from climate model simulations of the Deep-Time Model Intercomparison Project (DeepMIP[58,59]; Supplementary Fig. 3) for various pCO_2 concentrations. These provide constraints on (1) the Eocene background climate state at Messel and (2) the magnitude of the global carbon perturbation, although we acknowledge that using only one proxy location might introduce site-specific biases. Several pCO_2 scenarios ranging from 1× to 9× pre-industrial concentrations (PI) have been simulated, all using similar Eocene paleogeography and pre-industrial orbital configuration[58]. However, we, note that the latter would have had higher eccentricity during hyperthermal events compared to the pre-industrial configuration used in the DeepMIP simulations[5,40,58]. Simulated temperatures at Messel at 3× to 4× PI are all below the brGDGT-based Eocene pre- and post-Event background temperatures of 24.4 °C (Fig. 5), while temperature estimates from leaf margin analysis (21.7 ± 1.8–23.1 ± 1.9 °C) and the coexistence approach (16.8–23.9 °C)[46] prior the event, match the 3× to 4× simulations. Our brGDGT temperatures alone agree best with 6× PI (1680 ppm) simulations (Fig. 5), but considering proxy uncertainties and the spread in DeepMIP simulations due to e.g., differences in spatial resolution[58], it is also conceivable that pre- and post-Event atmospheric pCO_2 concentrations were likely around 3× to 4× PI which fits re-evaluated stomatal proxy data from Messel (pCO_2 concentrations of ~1149 ppm[36,60])

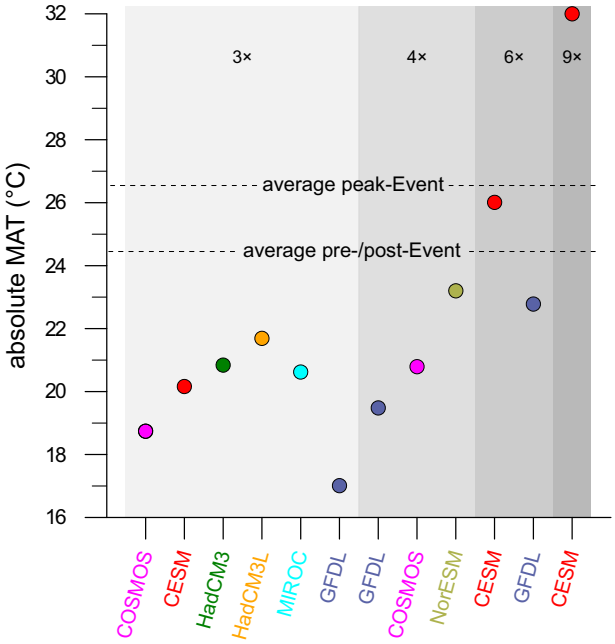

Fig. 5 | Proxy data comparison with simulated surface air temperature for the Eocene Messel site (~46° N, 6° E). Absolute local MAT simulations at various pCO_2 concentrations (3×, 4×, 6×, and 9× relative to preindustrial; PI). The color scheme represents different models. Average pre-/post hyperthermal and hyperthermal peak-event temperature is indicated by horizontal dashed lines. Temperature simulations are derived from the Deep-Time Model Intercomparison Project (DeepMIP). All models have comparable paleogeographic and vegetation boundary conditions. Solar constant and orbital configuration are set to preindustrial values. For details on model configurations see ref. 58.

and global pCO_2 estimates from that period[60]. Next, we assess the greenhouse gas contribution during the hyperthermal by evaluating temperature rise as a function of atmospheric pCO_2. Simulated temperature change to pCO_2 doubling is at least 3.9 °C (from 1× to 2× preindustrial pCO_2) at Messel and increases to a maximum of 5.8 °C (CESM and GFDL for 3× to 6× preindustrial pCO_2; Supplementary Fig. 4), which is above the maximum brGDGT-derived warming of 3.5 °C. We, therefore, posit that atmospheric pCO_2 increase during C21n-H1 was likely less than a doubling of the pre-Event pCO_2 levels, especially considering that orbital forcing played an additional role in the maximum warming.

Conclusions

With a total increase in brGDGT temperatures of up to 3.5 °C, the Eocene mid-latitude Messel maar lake provides a unique sub-millennial- to millennial-scale continental temperature record covering a post-PETM Eocene hyperthermal event (47.2 Ma). The high-resolution brGDGT and $\delta^{13}C$ records reveal two warming maxima during the peak-Event interval of the hyperthermal, indicating a nonlinear warming signal likely modulated by orbital forcing. Collectively, the Messel maar biomarker data highlight not only the magnitude of continental warming but also further emphasize that Central European temperatures also varied significantly (up to 3 °C) on shorter timescales (10^3–10^4 years) during this hyperthermal. The lacustrine $\delta^{13}C_{TOC}$ record mirrors the global benthic $\delta^{13}C$ stack indicating that the maar lake was a sensitive recorder of perturbations to the global carbon cycle. However, a rapid shift in algal communities and TOC during peak hyperthermal conditions resulted in $\delta^{13}C_{TOC}$ values lower than at any time within the ~650 ka record of the Messel maar lake. Moreover, the pCO_2 increase during the hyperthermal was likely less than a doubling relative to pre-Event levels as indicated by climate model simulations. We, therefore, document that even moderate hyperthermals relative to the PETM, with maximal warming of ca. 3.5 °C had a profound impact on terrestrial aquatic ecosystems. Projected global warming due to increasing anthropogenic greenhouse gas emissions might hence drive similar disruptions in lake ecosystems in the near future.

Methods

Study site and FB2001 drill core

The Eocene Messel maar lake (Fig. 1), is the remnant of a volcanic eruptive center filled by volcaniclastics and lacustrine sediments after an eruption, ca. 48 Ma ago[16]. In 2001, the FB2001 drill core recovered 433 m of maar sediments and the underlying volcanoclastic material from the center of the maar lake[25] (Fig. 1c). The uppermost ~94 m of the core comprises the Middle Messel Formation (MMF) and consists of a succession of finely-laminated, high TOC (average 27%) pelites[25,32]. The OM in the MMF is thermally immature[32] and consists of autochthonous (aquatic macrophytes and phytoplankton) and allochthonous (terrestrial higher plants) OM[18,32]. High TOC and laminations within the MMF indicate stable meromictic lake conditions with bottom anoxia prevailing during the accumulation of the MMF[25].

Geochemical analysis

All sample material in this study originates from sample splits of FB2001 that are part of the collections at the Senckenberg Research Institute and Natural History Museum Frankfurt. The latter also granted access to the sampling material. We analyzed 41 samples from the uppermost 12 m of the cored MMF (Fig. 1c, Supplementary Methods). Samples were freeze-dried at −56 °C for 24 h and subsequently powdered by mortar and pestle. Lipid biomarkers were solvent-extracted from ~1 g sediment via a Soxhlet apparatus. Total lipid extracts were separated by column chromatography over alumina into apolar and polar fractions using hexane:dichloromethane (9:1, *v:v*) and dichloromethane:methanol (1:1, *v:v*), respectively. The polar fraction was dissolved in hexane:*iso*-propanol (99:1, *v:v*), filtered (0.45 µm PTFE filter), and analyzed by high-performance liquid chromatography atmospheric pressure chemical ionization mass spectrometry (HPLC-APCI-MS) on a Shimadzu UFLC device coupled to an AB Sciex 3200QTrap. Polar analytes were separated by two UHPLC silica columns (2.1 × 150 mm, 1.7 µm; Waters) in series, connected to a 2.1 × 5 mm pre-column (Waters). Column temperature was 30 °C and flow rate was 0.2 ml × min^{-1}. GDGTs were eluted isocratically using 18% B for 25 min, then a linear gradient to 35% B in 35 min, followed by a ramp to 100% B in 30 min, where B is hexane/isopropanol (9:1; *v:v*) and A is hexane. The maximum obtained system pressure during analysis was 230 bar. Target molecules were measured in selected ion monitoring mode. Chromatographic peak areas were integrated manually using the Sciex Analyst software (Supplementary Fig. 5).

The carbon isotope composition of bulk OM ($\delta^{13}C_{TOC}$) and TOC (weight %) was measured on powdered samples using a Flash EA 1112 (Thermo Finnigan) coupled with a MAT 253 (Thermo Finnigan) at the Goethe University-Senckenberg BiK-F Joint Stable Isotope Facility, Frankfurt. Prior to the analysis, sample powders were reacted with 10% hydrochloric acid for 24 h at 70 °C in order to remove the carbonate component, then neutralized with ultra-pure water and dried for 3 days at 50 °C. Reference materials, USGS 24 and IAEH-CH 7 were measured on a daily basis and reference measurements resulted in a standard deviation between replicate measurements of <0.2‰ for $\delta^{13}C_{TOC}$ values. TOC concentrations were quantified by comparison of the signal size between samples and the standards with known carbon content. An error was typically within 0.5%. TOC values were not additionally corrected for weight loss during decalcification. However, the inorganic carbon content across the core section analyzed here was reported to be <1.6%[32]. Given the rather homogeneous carbonate content in the samples, we assume that potential uncertainty based on the absence of such a weight-loss correction is ≤1.6%.

brGDGT indices and temperature reconstruction

In order to quantify paleo-temperatures and water pH we calculated the Methylation of Branched Tetraether (MBT'_{5Me}) and the Cyclisation of

Branched Tetraether (CBT') indices[61]:

$$MBT'_{5Me} = (Ia + Ib + Ic)/(Ia + Ib + Ic + IIa + IIb + IIc + IIIa) \quad (1)$$

$$CBT' = 10_{log}[(Ic + IIa' + IIb' + IIc' + IIIa' + IIIb' + IIIc')/(Ia + IIa + IIIa)] \quad (2)$$

Roman numerals correspond to molecular brGDGT structures shown in Supplementary Fig. 6. The fractional abundance of branched- and isoprenoidal-GDGTs is shown in Supplementary Fig. 7. The MBT'_{5Me} is translated into MATs using the BayMBT calibration (RMSE = 2.9 °C)[20]. We applied this model due to (i) consideration of the improved chromatographic separation[62] (MBT'_{5Me}) relative to older calibrations[63], (ii) appropriate upper calibration limit of the BayMBT model (28.1 °C) while other calibrations provide temperature estimates that are off the limit when applied to Messel samples[19,63], (iii) stronger correlation statistics of the MBT'_{5Me} relative to MBT'_{6Me}[64] in the original BayMBT model study[20], and (iv) the use of an extended data set ($n = 272$) for constraining the BayMBT approach[20] (for details see Supplementary Discussion). We set the prior mean value in the BayMBT model to 18 °C based on previous MAAT reconstruction for the Eocene Messel site[65]. The prior standard deviation was 15 °C. Analytical reproducibility of the MBT'_{5Me} index was determined by running an in-house standard ($n = 5$) every six samples, resulting in an overall range of 0.011 for MBT'_{5Me} which would translate into a temperature error of ≤0.3 °C, negligible relative to the calibration error of the BayMBT model (RMSE: ±2.9 °C).

Lake water pH was calculated based on the CBT' index[19]:

$$pH = 8.95 + 2.65 * CBT' \quad (r^2 = 0.57, RMSE = 0.8) \quad (3)$$

Reporting summary

Further information on research design is available in the Nature Portfolio Reporting Summary linked to this article.

Data availability

All data presented in this study are available on PANGAEA. The DeepMIP Eocene climate model outputs are available by the following instructions at https://www.deepmip.org/data-eocene/.

Received: 28 February 2024; Accepted: 14 August 2024;
Published online: 29 August 2024

References

1. Bowen, G. J. et al. Eocene hyperthermal event offers insight into greenhouse warming. *Eos* **87**, 165–169 (2006).
2. Zachos, J. C., Dickens, G. R. & Zeebe, R. E. An early Cenozoic perspective on greenhouse warming and carbon-cycle dynamics. *Nature* **451**, 279–283 (2008).
3. Sexton, P. F. et al. Eocene global warming events driven by ventilation of oceanic dissolved organic carbon. *Nature* **471**, 349–353 (2011).
4. McInerney, F. A. & Wing, S. L. The paleocene–eocene thermal maximum: a perturbation of carbon cycle, climate, and biosphere with implications for the future. *Annu. Rev. Earth Planet. Sci.* **39**, 489–516 (2011).
5. Westerhold, T., Röhl, U., Donner, B. & Zachos, J. C. Global extent of early eocene hyperthermal events: a new pacific benthic foraminiferal isotope record from shatsky rise (ODP site 1209). *Paleoceanogr. Paleoclimatol.* **33**, 626–642 (2018).
6. Westerhold, T. et al. An astronomically dated record of Earth's climate and its predictability over the last 66 million years. *Science* **1387**, 1383–1387 (2020).
7. Frieling, J. et al. Thermogenic methane release as a cause for the long duration of the PETM. *Proc. Natl. Acad. Sci. USA* **113**, 12059–12064 (2016).
8. Kirtland Turner, S., Hull, P. M., Kump, L. R. & Ridgwell, A. A probabilistic assessment of the rapidity of PETM onset. *Nat. Commun.* **8**, 1–9 (2017).
9. Kirtland Turner, S. & Ridgwell, A. Recovering the true size of an Eocene hyperthermal from the marine sedimentary record. *Paleoceanography* **28**, 700–712 (2013).
10. Röhl, U., Westerhold, T., Bralower, T. J. & Zachos, J. C. On the duration of the Paleocene–Eocene thermal maximum (PETM). *Geochem. Geophys. Geosystems.* https://doi.org/10.1029/2007GC001784 (2007).
11. Sluijs, A. et al. Environmental precursors to rapid light carbon injection at the Palaeocene/Eocene boundary. *Nature* **450**, 1218–1221 (2007).
12. Tierney, J. E. et al. Spatial patterns of climate change across the Paleocene–Eocene thermal maximum. *Proc. Natl. Acad. Sci. USA* **119**, 1–7 (2022).
13. Frieling, J. et al. Extreme warmth and heat-stressed plankton in the tropics during the Paleocene–Eocene thermal maximum. *Sci. Adv*. **3**, e1600891 (2017).
14. Foster, G. L., Hull, P., Lunt, D. J. & Zachos, J. C. Placing our current 'hyperthermal' in the context of rapid climate change in our geological past. *Philos. Trans. R. Soc. A Math. Phys. Eng. Sci*. **376**, 20170086 (2018).
15. Tierney, J. E. et al. Past climates inform our future. *Science*. **370**, eaay3701 (2020).
16. Kaboth-Bahr, S. et al. Improved chronostratigraphy for the Messel formation (Hesse, Germany) provides insight into early to middle Eocene climate variability. *Newslett. Stratigr*. https://doi.org/10.1127/nos/2024/0799 (accepted 2024).
17. Hayes, J. M., Takigiku, R., Ocampo, R., Callot, H. J. & Albrecht, P. Isotopic compositions and probable origins of organic molecules in the Eocene Messel shale. *Nature* **329**, 48–51 (1987).
18. Goth, K., De Leeuw, J. W., Püttmann, W. & Tegelaar, E. W. Origin of Messel oil shale kerogen. *Nature* **336**, 759–761 (1988).
19. Russell, J. M., Hopmans, E. C., Loomis, S. E., Liang, J. & Sinninghe Damsté, J. S. Distributions of 5- and 6-methyl branched glycerol dialkyl glycerol tetraethers (brGDGTs) in East African lake sediment: effects of temperature, pH, and new lacustrine paleotemperature calibrations. *Org. Geochem.* **117**, 56–69 (2018).
20. Martínez-Sosa, P. et al. A global Bayesian temperature calibration for lacustrine brGDGTs. *Geochim. Cosmochim. Acta* **305**, 87–105 (2021).
21. Schoon, P. L. et al. Influence of lake water pH and alkalinity on the distribution of core and intact polar branched glycerol dialkyl glycerol tetraethers (GDGTs) in lakes. *Org. Geochem.* **60**, 72–82 (2013).
22. Inglis, G. N. et al. Biomarker approaches for reconstructing terrestrial environmental change. *Annu. Rev. Earth Planet. Sci.* **50**, 369–394 (2022).
23. Weber, Y. et al. Redox-dependent niche differentiation provides evidence for multiple bacterial sources of glycerol tetraether lipids in lakes. *Proc. Natl. Acad. Sci. USA* **115**, 10926–10931 (2018).
24. Lenz, O. K., Wilde, V., Mertz, D. F. & Riegel, W. New palynology-based astronomical and revised 40Ar/39Ar ages for the Eocene maar lake of Messel (Germany). *Int. J. Earth Sci.* **104**, 873–889 (2015).
25. Felder, M. & Harms, F. J. Lithologie und genetische Interpretation der vulkano-sedimentären ablagerungen aus der grube Messel anhand der forschungsbohrung Messel 2001 und weiterer Bohrungen. *Cour. Forsch. Inst. Senckenberg* **252**, 151–203 (2004).
26. Van Bree, L. G. J. et al. Seasonal variability and sources of in situ brGDGT production in a permanently stratified African crater lake. *Biogeosciences* **17**, 5443–5463 (2020).
27. So, R. T., Lowenstein, T. K., Jagniecki, E., Tierney, J. E. & Feakins, S. J. Holocene water balance variations in great salt lake, Utah: application

of GDGT Indices and the ACE salinity proxy. *Paleoceanogr. Paleoclimatol.* **38**, 1–18 (2023).
28. Tierney, J. E. & Russell, J. M. Distributions of branched GDGTs in a tropical lake system: Implications for lacustrine application of the MBT/CBT paleoproxy. *Org. Geochem.* **40**, 1032–1036 (2009).
29. Raberg, J. H. et al. Revised fractional abundances and warm-season temperatures substantially improve brGDGT calibrations in lake sediments. *Biogeosciences* **18**, 3579–3603 (2021).
30. Lenz, O. K., Wilde, V., Riegel, W. & Harms, F. J. A 600 k.y. record of El Niño-Southern oscillation (ENSO): evidence for persisting teleconnections during the Middle Eocene greenhouse climate of Central Europe. *Geology* **38**, 627–630 (2010).
31. Wu, J. et al. Variations in dissolved O_2 in a Chinese lake drive changes in microbial communities and impact sedimentary GDGT distributions. *Chem. Geol.* **579**, 120348 (2021).
32. Bauersachs, T., Schouten, S. & Schwark, L. Characterization of the sedimentary organic matter preserved in Messel oil shale by bulk geochemistry and stable isotopes. *Palaeogeogr. Palaeoclimatol. Palaeoecol.* **410**, 390–400 (2014).
33. Wang, H. et al. Biomarker-based quantitative constraints on maximal soil-derived brGDGTs in modern lake sediments. *Earth Planet. Sci. Lett.* **602**, 117947 (2023).
34. Weber, Y. et al. Identification and carbon isotope composition of a novel branched GDGT isomer in lake sediments: evidence for lacustrine branched GDGT production. *Geochim. Cosmochim. Acta* **154**, 118–129 (2015).
35. Mezger, J. E., Felder, M. & Harms, F. J. Crystalline rocks in the maar deposits of Messel: key to understand the geometries of the Messel Fault Zone and diatreme and the post-eruptional development of the basin fill. *Zeitschrift der Dtsch. Gesellschaft fur Geowissenschaften* **164**, 639–662 (2013).
36. Grein, M., Konrad, W., Wilde, V., Utescher, T. & Roth-Nebelsick, A. Reconstruction of atmospheric CO2 during the early middle Eocene by application of a gas exchange model to fossil plants from the Messel formation, Germany. *Palaeogeogr. Palaeoclimatol. Palaeoecol.* **309**, 383–391 (2011).
37. IPCC. Summary for Policymakers: Synthesis Report. In *Climate Change 2023 Synthesis Report. Contrib. Work. Groups I, II III to Sixth Assessment Report Intergovernmental Panel on Climate Change* 1–34 (IPCC, Switzerland, 2023).
38. Piedrahita, V. A. et al. Accelerated light carbon sequestration following late Paleocene-early Eocene carbon cycle perturbations. *Earth Planet. Sci. Lett.* **604**, 117992 (2023).
39. Inglis, G. N. et al. Mid-latitude continental temperatures through the early Eocene in western Europe. *Earth Planet. Sci. Lett.* **460**, 86–96 (2017).
40. Kiehl, J. T., Shields, C. A., Snyder, M. A., Zachos, J. C. & Rothstein, M. Greenhouse- and orbital-forced climate extremes during the early Eocene. *Philos. Trans. R. Soc. A Math. Phys. Eng. Sci*. **376**, 20170085 (2018).
41. Lawrence, K. T., Sloan, L. C. & Sewall, J. O. Terrestrial climatic response to precessional orbital forcing in the Eocene. *Spec. Pap. Geol. Soc. Am* **369**, 65–77 (2003).
42. Lenz, O. K., Wilde, V. & Riegel, W. ENSO- and solar-driven sub-Milankovitch cyclicity in the Palaeogene greenhouse world; high-resolution pollen records from Eocene lake Messel. *Germany. J. Geol. Soc. London.* **174**, 110–128 (2017).
43. Berger, A., Loutre, M. F. & Mélice, J. L. Climate of the past equatorial insolation: from precession harmonics to eccentricity frequencies *. *Clim. Past* **2**, 131–136 (2006).
44. De Vleeschouwer, D., Da Silva, A. C., Boulvain, F., Crucifix, M. & Claeys, P. Precessional and half-precessional climate forcing of mid-Devonian monsoon-like dynamics. *Clim. Past* **8**, 337–351 (2012).
45. Ulfers, A., Zeeden, C., Voigt, S., Sardar Abadi, M. & Wonik, T. Half-precession signals in Lake Ohrid (Balkan) and their spatio-temporal relations to climate records from the European realm. *Quat. Sci. Rev.* **280**, 107413 (2022).
46. Grein, M., Utescher, T., Wilde, V. & Roth-Nebelsick, A. Reconstruction of the middle Eocene climate of Messel using palaeobotanical data. *Neues Jahrb. Geol. Palaontol. Abh.* **260**, 305–318 (2011).
47. Bowen, G. J. Up in smoke: a role for organic carbon feedbacks in Paleogene hyperthermals. *Glob. Planet. Change* **109**, 18–29 (2013).
48. Meyers, P. A. & Ishiwatari, R. Lacustrine organic geochemistry-an overview of indicators of organic matter sources and diagenesis in lake sediments. *Org. Geochem.* **20**, 867–900 (1993).
49. Meyers, P. A. Application of organic geochemistry to paleolimnological reconstruction: a summary of examples from the laurention great lakes. *Org. Geochem.* **34**, 261–289 (2003).
50. Freeman, K. H. & Hayes, J. M. Evidence from carbon isotope measurements for diverse origins. *Nature* **343**, 1–18 (1990).
51. Lücke, A., Schleser, G. H., Zolitschka, B. & Negendank, J. F. W. A lateglacial and Holocene organic carbon isotope record of lacustrine palaeoproductivity and climatic change derived from varved lake sediments of Lake Holzmaar, Germany. *Quat. Sci. Rev.* **22**, 569–580 (2003).
52. Heyng, A. M. et al. Environmental changes in northern New Zealand since the middle Holocene inferred from stable isotope records (δ 15N, δ 13C) of Lake Pupuke. *J. Paleolimnol* **48**, 351–366 (2012).
53. Street-Perrott, F. A. et al. The Holocene isotopic record of aquatic cellulose from Lake Äntu Sinijärv, Estonia: influence of changing climate and organic-matter sources. *Quat. Sci. Rev.* **193**, 68–83 (2018).
54. Richter, G., Schiller, W. & Baszio, S. A green alga of the genus Coelastrum Naegeli from the sediments of the tertiary lake Messel. *Palaeobiodivers. Palaeoenviron.* **93**, 285–298 (2013).
55. Carmichael, M. J. et al. A model-model and data-model comparison for the early Eocene hydrological cycle. *Clim. Past* **12**, 455–481 (2016).
56. Beaulieu, J. J. et al. Effects of an experimental water-level drawdown on methane emissions from a eutrophic reservoir. *Ecosystems* **21**, 657–674 (2018).
57. Harrison, J. A., Deemer, B. R., Birchfield, M. K. & O'Malley, M. T. Reservoir water-level drawdowns accelerate and amplify methane emission. *Environ. Sci. Technol.* **51**, 1267–1277 (2017).
58. Lunt, D. J. et al. DeepMIP: model intercomparison of early Eocene climatic optimum (EECO) large-scale climate features and comparison with proxy data. *Clim. Past* **17**, 203–227 (2021).
59. Lunt, D. J. et al. The DeepMIP contribution to PMIP4: experimental design for model simulations of the EECO, PETM, and pre-PETM (version 1.0). *Geosci. Model Dev.* **10**, 889–901 (2017).
60. Hönisch, B. et al. Toward a Cenozoic history of atmospheric CO2. *Science* **382**, eadi5177 (2023).
61. De Jonge, C. et al. Occurrence and abundance of 6-methyl branched glycerol dialkyl glycerol tetraethers in soils: implications for palaeoclimate reconstruction. *Geochim. Cosmochim. Acta* **141**, 97–112 (2014).
62. Hopmans, E. C., Schouten, S. & Sinninghe Damsté, J. S. The effect of improved chromatography on GDGT-based palaeoproxies. *Org. Geochem.* **93**, 1–6 (2016).
63. Pearson, E. J. et al. A lacustrine GDGT-temperature calibration from the scandinavian Arctic to Antarctic: renewed potential for the application of GDGT-paleothermometry in lakes. *Geochim. Cosmochim. Acta* **75**, 6225–6238 (2011).
64. Dang, X. Y., Xue, J. T., Yang, H. & Xie, S. C. Environmental impacts on the distribution of microbial tetraether lipids in Chinese lakes with contrasting pH: implications for lacustrine paleoenvironmental reconstructions. *Sci. China Earth Sci.* **59**, 939–950 (2016).
65. Tütken, T. Isotope compositions (C, O, Sr, Nd) of vertebrate fossils from the middle Eocene oil shale of Messel, Germany:

implications for their taphonomy and palaeoenvironment. *Palaeogeogr. Palaeoclimatol. Palaeoecol.* **416**, 92–109 (2014).
66. Schlitzer, R. Ocean Data View (2023).
67. Knox, R. W. O. B. et al. Cenozoic. In *Petroleum Geological Atlas of the Southern Permian Basin Area* (eds. Dornenbaal, H. & Stevenson, A.) 211–223 (EAGE Publications, 2010).

Acknowledgements

This research was funded through the VeWA consortium (Past Warm Periods as Natural Analogs of our high-CO_2 Climate Future) by the LOEWE program of the Hessen Ministry of Higher Education, Research and the Arts, Germany. We thank Ulrich Treffert and Karin Schmidt for their technical support. A.B. and S.K.-B. acknowledge funding by the German Research Foundation via projects BA 3809/16-1, KA 4757/7-1, respectively. We also acknowledge the efforts of the DeepMIP community and are thankful for the available model outputs. We thank three anonymous reviewers for their suggestions and constructive comments that improved the manuscript.

Author contributions

C.S., I.V., N.M., and A.M. designed the study. C.S. collected samples, conducted geochemical analyses, and performed brGDGT-based temperature estimates. C.S. drafted the manuscript with major input from I.V., N.M., and A.M. J.B. analyzed the climate simulations. S.K.-B. and A.B. helped with data interpretation and revised the manuscript. I.V. and A.M. supervised the project. All co-authors contributed to interpreting the data and writing the paper.

Funding

Open Access funding enabled and organized by Projekt DEAL.

Competing interests

The authors declare no competing interests.

Additional information

Supplementary information The online version contains supplementary material available at https://doi.org/10.1038/s43247-024-01628-9.

Correspondence and requests for materials should be addressed to Clemens Schmitt.

Peer review information *Communications Earth & Environment* thanks the anonymous reviewers for their contribution to the peer review of this work. Primary Handling Editors: Olivier Sulpis and Carolina Ortiz Guerrero. A peer review file is available.